Terahertz Imaging Unravels the Role of Nanoparticle Distribution in Magnetic Scaffolds for RF Hyperthermia

Matteo Bruno Lodi, Sonia Zappia, Nicola Curreli, Rosa Scapaticci, Ilaria Catapano, Alessandro Fanti, Lorenzo Crocco, and Giuseppe Mazzarella

Abstract – Magnetic scaffolds are magnetoresponsive biomedical devices combining magnetic nanoparticles and biomaterials. These devices are implanted after reductive surgery and are used to treat bone cancers by performing interstitial hyperthermia treatment, applying RF magnetic fields. Despite the promising therapeutic potential, magnetic scaffold loading can drastically affect the treatment outcome. In this work, an extensive characterization of 10 samples was conducted. Terahertz time-of-flight imaging was used to derive spatial distributions of the nanoparticles in the biomaterial and to perform advanced numerical simulations to study the effect on the hyperthermia treatment of residual bone cancer cells. We found that the temperature in the target tumor region was linearly correlated with the homogeneity of the magnetic nanoparticle distribution, while being inversely related to its skewness and nonlinearly related to its kurtosis.

1. Introduction

Bone tumors (BTs) are hard tissue neoplasms with 30% to 40% 5 year survival rates, causing pain and pathologic fractures, while being insensitive to chemotherapy and radiation [1]. BTs are treated with limb-sparing or reductive surgery [2], but a recurrence rate of ∼40% is reported [1, 2]. Thus, new effective therapeutic approaches are required. In oncology, hyperthermia treatment (HT) can supplement existing treatments by raising the temperature T of a target tissue in the range of 40 °C to 44 °C for at least 60 min [3, 4], increasing chemotherapeutics and radiotherapy effectiveness [4]. Electromagnetic (EM) energy at various frequencies is used to carry out HT; RF (100 kHz to 100 MHz) and microwaves (MW; 300 MHz to 300 GHz) are used to heat pathological tissues [2–4]. RF HT is clinically appealing because deep sites and antenna array design challenge MW thermal therapies. For BTs, MW HT has drawbacks of poor clinical improvement and damaging healthy bone tissue [2], requiring bone graft implantation [4]. Healthy bone weakening requires artificial biomaterial implants for postoperative mechanical stability [3].

Recently, new engineering methods enabling EM-based HT, while accounting for mechanical and biocompatibility features, were proposed. Magnetic nanoparticles (MNPs) are loaded into a polymeric or ceramic biomaterial to obtain a magnetic scaffold (MS) [4–6]. MSs are nanocomposite multifunctional magnetoresponsive biomaterials [4–6] to be implanted after BT removal and to be exposed to an external RF magnetic field to allow the MNPs in the biomaterial to dissipate therapeutic heat and perform HT against residual BT cells (Figure 1). This new RF HT modality would change the landscape of orthopedic oncology [3–7]. Despite potential for MS in the available literature, present techniques are limiting and must be carefully examined. The material science point of view is dominating. Also, empirically driven manufacture and use of MS not well supported by modeling or quantitative engineering reasons are observed. For BT HT with MS, success is mainly determined by the magnetic properties of the MS. For MS, the manufacturing method, the biomaterial geometry, and architecture (e.g., porosity, tortuosity) can have significant impacts on the RF power deposition and HT outcome [5, 6]. Recently, the importance of porosity in a 3D-printed ferromagnetic MS was highlighted [6]. How the MNP amount and loading pattern can affect RF HT with MS must be clarified. Physical methods for producing MS, such as impregnation or dip coating, can cause a 20% variance in saturation magnetization in a 5 mm volume [7]. In [5], for the first time, we characterized MS using terahertz (THz) time-of-flight (ToF) imaging to determine the MNP distribution. We demonstrated that MS loading might affect the HT outcome. However, no design principles or quantitative laws for driving the impregnation or dip coating of biopolymers with MNPs have been developed from [5]. In this work, we used the THz ToF images of the 10 dip-coated MS having inhomogeneous MNP distribution from [5] to perform unique and novel advanced numerical simulations and correlate the HT outcome with THz ToF image features

Manuscript received 3 January 2024. Research funding from the European Union, NextGenerationEU, through the Italian Ministry of University and Research (PNRR-M4C2-I1.3 Project PE_00000019 "Heal Italia") was awarded to Matteo Bruno Lodi and Alessandro Fanti (CUP F53C22000750006, University of Cagliari). The views and opinions expressed are those of the authors only and do not necessarily reflect those of the European Union or the European Commission. Neither the European Union nor the European Commission are held responsible for them.

Matteo Bruno Lodi, Alessandro Fanti, and Giuseppe Mazzarella are with the Department of Electrical and Electronic Engineering, University of Cagliari, Via Marengo 3, 09123 Cagliari, Italy; e-mail: matteob.lodi@unica.it.

Sonia Zappia, Rosa Scapaticci, Ilaria Catapano, and Lorenzo Crocco are with the Institute for the Electromagnetic Sensing of the Environment, National Research Council of Italy, 80124 Naples, Italy.

Nicola Curreli is with the Functional Nanosystems, Istituto Italiano di Tecnologia, via Morego 30, 16163 Genova, Italy.

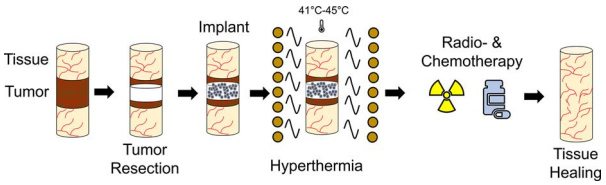

Figure 1. Concept of MSs as innovative tools for administering local, interstitial hyperthermia against residual BT cells, following surgical resection and implantation.

to elucidate how the MNPs homogeneity and asymmetry can affect the quality of the RF HT of BT with MS.

2. Model: Geometry and EM–Thermal Problems

We consider a sample case study of a layered surface phantom of a human arm (Figure 2) when a BT was surgically removed [4]. MS with a radius of $r_{sc} = 5$ mm was implanted (Figure 2). The surgical excision left a 0.5 mm thick margin of remaining BTs. The other tissue layers were skin ($t_s = 1.5$ mm), fat ($t_f = 10$ mm), and muscle ($t_m = 36$ mm). The bone humerus radius was $r_{\text{bm}} + t_b = 20$ mm thick, while the bone marrow (BM) radius was $r_{\text{bm}} = 10$ mm.

The system was exposed to a RF MF produced by a solenoid operating at a frequency $f = 300$ kHz, with strength 30 mT. The field is deactivated at $t = 80$ min. The distribution of electric $\boldsymbol{E}$ and magnetic $\boldsymbol{H}$ fields was determined using the MS, tissues, and EM properties taken from [4]. The total EM power per volume unit that dissipated during the HT in the system was $Q_{\text{EM}} = P_e + P_m$. The heat due to the induced RF currents was $P_e = \frac{1}{2}\sigma|\boldsymbol{E}|^2$, where σ is the electrical conductivity (Sm^{-1}) [4]. The magnetic losses due to the implanted MS (P_m) were computed as $P_m = \pi\mu_0 f|\boldsymbol{H}|^2\chi''$ [4], where μ_0 is the vacuum magnetic permeability and χ'' is the imaginary part of the magnetic susceptibility of the MS, described by the Cole–Cole model [4]. If MNPs are monodisperse, the static susceptibility χ_0 linearly depends on the MNPs volume fraction in the biomaterial ϕ_m and the saturation magnetization M_s (Am^{-1}), while depending nonlinearly from the particle volume and T [4, 5]. The Néel relaxation time (τ_N) is a nonlinear function of temperature [5]. By focusing on ϕ_m, M_s, a clarification is in order. Usually, ϕ_m is the volume-averaged amount of MNPs in the biomaterial. However, this assumption can lead to misleading estimations of the HT parameters and an erroneous prediction of its therapeutic outcome [5]. The term ϕ_m depends on the processing and manufacturing conditions and $\phi_m \neq \text{const}$ in the biomaterial volume so that $\phi_m = \widetilde{\phi}_m\phi(x,y)$, where $\widetilde{\phi}_m$ is the peak value and $\phi(x,y)$ is an unknown distribution. Therefore, $P_m = P_m\ (x,y)$, due to dependence from $\boldsymbol{H}$, T, but also from $\phi(x,y)$. However, the problem of obtaining the unknown $\phi(x,y)$ to accurately solve the nonlinear EM–thermal model is underestimated. M_s mapping [7], destructive microscopy tests, costly magnetic resonance imaging analyses, and low-resolution magnetic particle imaging were proposed [5]. We used THz ToF as a nondestructive characterization tool for MS for the first time [5], demonstrating that the sample thickness, refractivity index, and MNP distribution map could be calculated. We will present, explain, and apply this approach to obtain $\phi(x,y)$, perform advanced numerical simulations, and conduct a revised quantitative analysis to evaluate how MNPs loading pattern affects the HT outcome in this work.

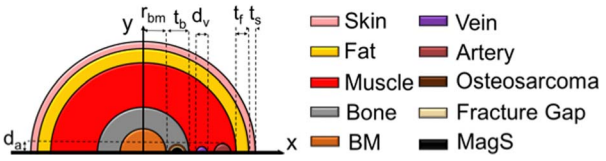

Figure 2. System geometry: the x-axis symmetric surface phantom of the human arm, with a resected BT and MS implanted.

The RF HT was modeled by solving the Pennes bioheat equation (PBHE) [4]. The unsteady PBHE was solved considering the initial condition $t = 0$ min, $T = T_0$. As boundary conditions, we assume heat exchange by free convection at the skin–air interface (7.7 $\text{Wm}^{-2}\text{K}^{-1}$). At the muscle–vessel interface, an effective convection mechanism was assumed [4]. The thermal properties, taken from [4], especially the blood perfusion of healthy and tumor tissues, strongly depends upon T [4]. Therefore, the thermal conductivity k and the specific heat C_p were assumed to vary linearly with T [4]. The frequency–transient numerical framework from [4] was used to the solve the Maxwell equations and the heat transfer balance in Comsol Multiphysics version 5.5 (Comsol Inc., Burlington, Massachusetts). The temperature attained in 50% of the target BT volume (T_{50}) was calculated and examined [5].

3. Materials and Characterization

The cubic and cubo-octahedral magnetic iron oxide nanocrystals (Fe_3O_4, γ-Fe_2O_3), synthesized by modified partial oxidation pathway [5], were loaded in polycaprolactone (PCL) scaffolds (3D Biotek LLC, Warren, New Jersey) [5]. The diameter and height of the 90°-interlaced fiber (300 μm in diameter and spacing, ~80% porosity) PCL disks are 5 mm and 1.6 mm, respectively. The modified dip-coating method was used to create the MS [5]. The MNP dispersion was deposited on the scaffolds using a NdFeB permanent magnet (S-20-20-N, Webcraft GmbH, Gottmadingen, Germany; Figure 3), forcing MNP uptake. Ten MS samples were manufactured (Figure 3). The technique was carried out for samples M1 to M6 to obtain homogeneous distributions of MNPs in the PCL

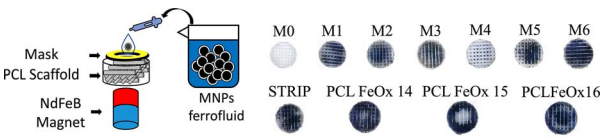

Figure 3. Schematic representation of the manufacturing procedure and optical images of 10 samples of the manufactured MSs.

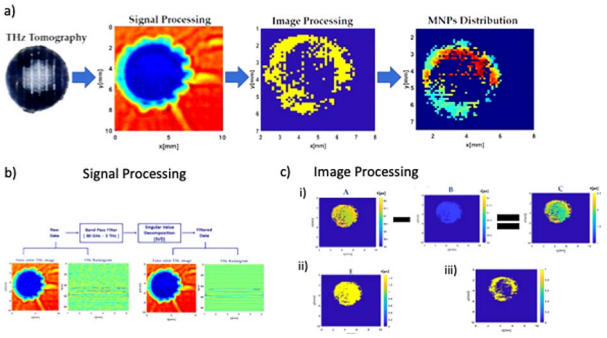

Figure 4. (a) Overall pipeline for the THz-based characterization of MSs. (b) Filtering and processing of the THz signals. (c) Image processing procedures.

volume. For the MS identified as strip and PCL14 to PCL16, a water-repellent tape with a specific pattern was placed to one side of the PCL to limit MNP deposition and achieve an inhomogeneous distribution of MNPs. Two families of MS can be distinguished: samples M1 to M6 have MNPs with a ∼58 nm crystalline domain, while strip and PCL14 to PCL16 MS samples have MNPs of ∼32 nm in average size. Large MNP aggregates (∼10 μm to 40 μm in size) were observed [5].

Static magnetic characterizations were carried out using the SQUID MPMS XL EverCool (Quantum Design, Rome, Italy) instrument for $\mu_0 H \in [-7, 7]$T, $T = 37$ °C, and the magnetization curves were fitted with MATLAB version 2021a (MathWorks, Natick, Massachusetts) to derive ϕ_m.

4. THz Imaging

We proposed an approach to create a 2D map of the MNP distribution [5, 8]. The time of flight t_f (pico-seconds) THz signal within the MS was compared with the propagation time signal obtained in a bare, not loaded PCL sample ($t_{f,\text{ref}}$). The 2D differential propagation delay map (PDM) $PDM = t_f - t_{f,\text{ref}}$ was obtained (Figure 4c) [8], accounting for the time delay introduced by MNPs. From the PDM, we estimated a quantity encoding the amount of MNPs in the MS under testing called the *magnetization index* (I_m), computed as the ratio between the number of pixels ($p_{n,m}$) containing MNPs and the total number of pixels discretizing the scanning area and intercepting the sample ($S \in N$), with $N \times M$ as the image size. A threshold value ($t_{f,\text{th}}$) was estimated by considering the difference between two references t_f (i.e., the difference between $t_{f,\text{ref}}$ and the propagation time obtained for a MS homogeneously loaded with MNPs). The value $t_{f,\text{th}}$ was used as a threshold for the PDM ($PDM/t_{f,\text{th}}$) and to obtain a binary magnetization map called the *magnetization distribution mask* (MDM).

In the MDM map, $p_{n,m} > t_{f,\text{th}} = 1$, because the presence of the MNPs significantly affected the THz signal propagation. The MDM map enabled estimation of a magnetization distribution index (I_{md}) by considering the areas of the scaffolds, where the MNPs were mostly concentrated, i.e., as the ratio between the number of pixels, where $t_f > t_{f,\text{th}}$ and the total number of pixels. Finally, the 2D MNP distribution map was derived by performing the pixel-by-pixel multiplication of the binary MDM and the t_f-filtered THz signal amplitude (Figure 4c). These maps enabled visualizing where MNPs were mostly concentrated, allowing to quantitatively investigate $\phi(x, y)$.

The loading pattern $\phi(x, y)$ was obtained from the THz characterization by fitting MDM to a finite series of radial basis functions (RBFs) with the least-square method in MATLAB [5]. We used the RBFs to solve the EM model and PBHE. We advanced the analysis from [5], by refining the description of the MNP distribution. We post-processed the ToF images to extract features and distribution descriptors to be used in the following. In detail, we extracted the scaffold boundaries using a 2×2 Gaussian filter and Otsu thresholding, deriving the centroid and cropping the images to the MS region of interest, to analyze the first-order statistics features of the 2D MNP distribution for the MS. We extracted the range as $R_a = \max\{t_f\} - \min\{t_f\}$, the mean and the standard deviation [9], and computed the homogeneity (ψ) as the ratio of the mean and standard deviation value ($\psi = \bar{t}_f/\sigma_{t_f}$).We also considered the skewness (S_k) and the kurtosis [9]. Using the T_{50} from HT simulations and the MNP distribution features, we investigated any quantitative relationship to describe or predict the HT outcome of the 10 MS samples by relying on THz data.

Table 1. Fitting of magnetic measurements data and descriptors of ToF postprocessed images

Sample	M_{sc} (emu/g)	ϕ_m (%)	T_{50} (°C)	$\sigma_{T_{50}}$ (°C)	R_a (ps)	$\bar{t}_f$ (ps)	σ_{t_f} (pf)	ψ (arbitrary units)	S_k (arbitrary units)	K_u (arbitrary units)	I_m (arbitrary units)
M1	1.46	1.99	38.75	1.63	30.07	5.84	4.89	1.19	1.16	2.50	0.46
M2	1.01	1.36	37.96	0.33	23.16	3.72	3.48	1.07	1.41	3.18	0.30
M3	2.67	3.66	41.78	1.81	27.42	6.55	4.54	1.44	0.80	1.89	0.05
M4	1.92	2.63	40.00	1.15	30.87	3.07	4.07	0.75	2.32	6.55	0.14
M5	1.40	1.90	40.90	1.51	29.11	5.34	4.52	1.18	1.24	2.80	0.46
M6	8.66	12.10	42.98	2.31	40.73	40.59	4.71	2.26	0.001	1.54	0.66
PCL14	2.61	2.01	40.55	1.37	23.82	6.39	3.73	1.71	0.51	1.61	0.80
PCL15	1.96	2.38	40.24	1.28	28.42	6.22	4.32	1.43	0.92	2.32	0.49
PCL16	7.04	8.46	42.15	2.46	28.79	461	4.00	1.16	1.30	3.01	0.34
Strip	1.66	2.02	39.82	1.41	29.44	5.48	4.30	1.27	1.04	2.32	0.45

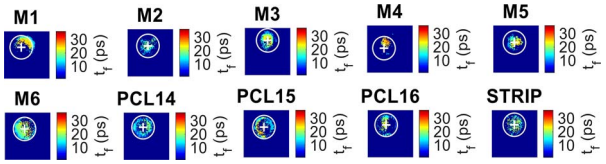

Figure 5. ToF maps of the 10 MS samples. The white line represents the segmented MS edge region, and the white cross is the estimated centroid of the scaffold.

5. Results and Discussion

The findings of the static magnetic measurements are reported in Table 1. M6 and PCL16 exhibit the highest M_{sc} and ϕ_m values. From Table 1, we note that $\phi_m \in [1.3, 12.1]$ and $M_{sc} \in [1.4, 8.6]$ emu/g. These findings are coherent with thermogravimetric analysis from [5]. The manufactured MS present a large variation for ϕ_m and M_{sc}. The ToF maps were processed, filtered, and elaborated to identify the MS (Figure 5) and derive the statistics descriptors reported in Table 1. From Table 1 and Figure 5, we notice that the higher the content of MNPs in the MS, the larger the $\bar{t}_f$, thus implying that a nonlinear relationship exists between these two quantities. Similarly, M_{sc} is positively correlated with $\bar{t}_f$. The maps reported in Figure 5 were used in silico to study how the 10 manufactured MS samples would perform in battling BTs with RF HT. The HT numerical simulations findings are reported in Figure 6. The RF heating is very localized (Figure 6a), being restricted to MS and the surrounding tissues. The deposited RF power in the MS is influenced by the MNP distribution, possibly resulting in asymmetric and uncontrollable heating patterns. Considering T_{50} in the tumor region (Figure 6b), almost all the MS (not M1 and M2) can perform an effective HT against BTs using a 300 kHz and 30 mT RF field. Considering the average $T_{50}(t)$ in the nontarget tissues, the bone and BM can experience a $\sim$1.5 °C temperature increase (Figure 6c) [5].

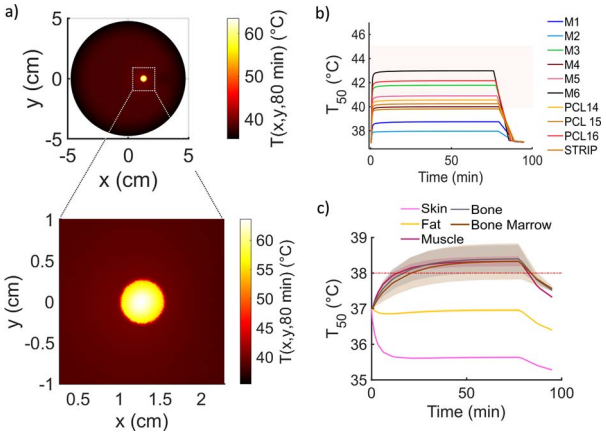

Figure 6. (a) Simulated 2D temperature distribution (in degrees Celsius) at $t = 80$ min (sample M6). (b) The $T_{50}(t)$ in the tumor region for the drop-casted MS. (c) Temperature (in degrees Celsius $\pm$ standard deviation for all MS) in the healthy tissues during the HT.

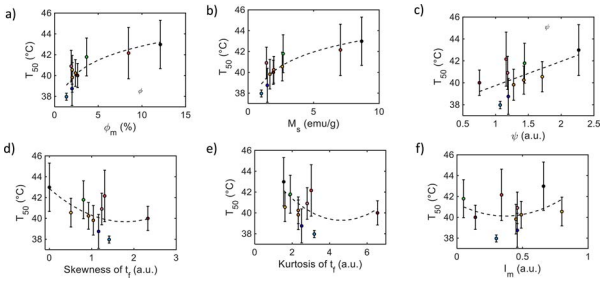

Figure 7. (a) The T_{50} versus magnetic phase amount. (b) The T_{50} versus saturation magnetization. (c) The T_{50} versus MNPs homogeneity. (d) The T_{50} as a function of skewness of the ToF distribution. (e) The T_{50} as a function of kurtosis of the ToF distributions. (f) The T_{50} as a function of the magnetization index.

By correlating the peak value of $T_{50}(t)$, linked to the HT quality, to ϕ_m and M_{sc}, we find that a nonlinear, power law relationship exists between these quantities (Table 1 and Figures 7a and 7b). However, considering the T_{50} variability in the tumor region, we highlight that the knowledge of the magnetic features is not sufficient to accurately predict the HT outcome, because the MNP distribution strongly influences the HT. Relying on ToF data, we investigated how the homogeneity, skewness, and kurtosis of the MNPs patterns correlate with T_{50}. We also investigated if I_m could be related the HT quality. For the homogeneity of MNPs (ψ), a weak linear positive correlation was found (Figure 7c). MS with lower ψ are associated with lower T_{50} values. In Figure 7d, a nonlinear trend of T_{50} from skewness S_k has been identified. Because skewness is linearly correlated to the homogeneity and considering an inverse quadratic dependence of T_{50} from S_k, we infer that less asymmetry is correlated to higher temperatures in the tumor volume. Note that as the kurtosis (K_u) decreases, the homogeneity is higher (Table 1), and mostly larger T_{50} values are found but with a larger standard deviation inside the target region. Finally, for I_m, we did not find any correlation with T_{50}, thus restraining the use of I_m as a morphological quantity.

6. Conclusion

New MS for RF HT has the potential to significantly alter the interventional scenario in clinical orthopedics and oncology, avoiding limb-sparing surgery and improving the efficacy of chemotherapy and radiotherapy. The current state of research does not address how manufacturing nonlinearities, such as the inhomogeneous loading of MNPs in the biomaterial, affect HT quality. We study this underappreciated element using characterization and modeling approaches from the EM engineering field. To fill this knowledge gap, we performed characterization on 10 dip-coated MSs with inhomogeneous patterns of MNPs. The MNP distribution in the biomaterial was determined using THz ToF imaging and was used to run advanced numerical nonlinear multiphysics simulations of the HT of BTs using MS. We correlated HT simulations and THz data and discovered that tumor temperature was directly associated with MNP distribution homogeneity, inversely related to

skewness, and nonlinearly related to kurtosis. Our findings can foster the design and manufacturing of MS for an effective and high-quality HT.

7. References

1. H. Katsuhiro and H. Tsuchiya, "The Role of Surgery in the Treatment of Metastatic Bone Tumor," *International Journal of Clinical Oncology*, **27**, February 2022, pp. 1238-1246.
2. K. Han, P. Dang, N. Bian, X. Chen, T. Yang, et al., "Is Limb Salvage With Microwave-Induced Hyperthermia Better Than Amputation for Osteosarcoma of the Distal Tibia?" *Clinical Orthopaedics and Related Research*, **475**, 6, June 2017, pp. 1668-1677.
3. M. Miola, Y. Pakzad, S. Banijamali, S. Kargozar, C. Viale-Brovarone, et al., "Glass-Ceramics for Cancer Treatment: So Close, or Yet so Far?" *Acta Biomaterialia*, **83**, January 2019, pp. 55-70.
4. M. B. Lodi, A. Fanti, G. Muntoni and G. Mazzarella, "A Multiphysic Model for the Hyperthermia Treatment of Residual Osteosarcoma Cells in Upper Limbs Using Magnetic Scaffolds," *IEEE Journal on Multiscale and Multiphysics Computational Techniques*, **4**, December 2019, pp. 337-347.
5. M. B. Lodi, N. Curreli, S. Zappia, L. Pilia, M. F. Casula, et al., "Influence of Magnetic Scaffold Loading Patterns on Their Hyperthermic Potential Against Bone Tumors," *IEEE Transactions on Biomedical Engineering*, **69**, 6, June 2022, pp. 2029-2040.
6. M. B. Lodi, A. Makridis, N. M. Carboni, K. Kazeli, N. Curreli, et al., "Design and Characterization of Magnetic Scaffolds for Bone Tumor Hyperthermia," *IEEE Access*, **10**, 2022, pp. 19768-19779.
7. A. Riminucci, C. Dionigi, C. Pernechele, G. De Pasquale, T. de Caro, et al., "Magnetic and Morphological Properties of Ferrofluid Impregnated Hydroxyapatite/Collagen Scaffolds," *Science of Advanced Materials*, **6**, 12, December 2014, pp. 2679-2687.
8. S. Zappia, R. Scapaticci, M. B. Lodi, A. Fanti, G. Ruello, et al., "Non-Destructive Characterization of Magnetic Polymeric Scaffolds Using Terahertz Time-of-Flight Imaging," *IEEE Transactions on Terahertz Science and Technology*, **13**, 4, July 2023, pp. 305-315.
9. A. Bilal, A. Serir, and Y. Chahir, "Feature Extraction in Palmprint Recognition Using Spiral of Moment Skewness and Kurtosis Algorithm," *Pattern Analysis and Applications*, **22**, 3, August 2019, pp. 1197-1205.